JOURNALS | Journal of Collective Sciences and Sustainability

Volume 1 Issue 2 (September 2025)
J. Collect. Sci. Sustain., 2025, 1(2), 25407
DOI : https://doi.org/10.64189/css.25407

Research Article

OPEN ACCESS

Directional Stability and Optimized Radar Cross-Section in Tailless Unmanned Aerial Vehicles

Shaik Aadil Iftikhaar,* Md. Akhtar Khan and Pritee Parwekar

School of Technology, GITAM University, GITAM Deemed to be University, Hyderabad, Telangana, 502329, India

*Corresponding Author
Shaik Aadil Iftikhaar
ashaik39@gitam.in

Received: 26 June 2025
Revised: 18 August 2025
Accepted: 08 September 2025
Published Online: 10 September 2025

Citation

S. A. Iftikhaar, M. A. Khan, P. Parwekar, Directional stability and optimized radar cross-section in tailless unmanned aerial vehicles, *Journal of Collective Sciences and Sustainability*, 2025, 1(2), 25407, doi: https://doi.org/10.64189/css.25407

Open Access

This article is licensed under a Creative Commons Attribution-NonCommercial 4.0 International License, which permits the non-commercial use, sharing, adaptation, distribution and reproduction in any medium or format, as long as appropriate credit to the original author(s) and the source is given by providing a link to the Creative Commons License and changes need to be indicated if there are any. The images or other third-party material in this article are included in the article's Creative Commons License, unless indicated otherwise in a credit line to the material. If material is not included in the article's Creative Commons License and your intended use is not permitted by statutory regulation or exceeds the permitted use, you will need to obtain permission directly from the copyright holder. To view a copy of this License, visit: https://creativecommons.org/licenses/by-nc/4.0/

© The Author(s) 2025

Abstract

This study presents the development of a tailless flying wing unmanned aerial vehicle (UAV) optimized for low radar cross-section (RCS) and enhanced aerodynamic stability. The design is based on Ludwig Prandtl's 1933 theory of induced drag minimization using a bell-shaped lift distribution, implemented through geometric and/or aerodynamic wing twist. By eliminating traditional vertical stabilizers and redistributing lift along the span, the configuration naturally counters adverse yaw and reduces dependency on active yaw control systems. The result is a structurally efficient UAV capable of stable flight, high payload capacity, and minimal radar signature. This makes it highly suitable for defense applications such as intelligence, surveillance, and reconnaissance (ISR), as well as strategic missions requiring endurance and stealth. Simulation results confirm that the proposed configuration achieves improved lift distribution, reduced induced drag, and enhanced directional stability compared to conventional tailless designs.

Keywords: Adverse yaw control; Stability; Bell-shaped lift distribution; Radar cross-section; Tailless UAV; Payload capacity.

1. Introduction

Tailless aircrafts face significant challenges in directional stability due to the absence of vertical stabilizers. A primary issue is adverse yaw, which occurs during roll maneuvers when differential lift and drag between wings cause the aircraft to yaw opposite to the turn.[1] In conventional aircraft, this is corrected by a vertical fin; however, in tailless designs as shown in Fig. 1, such correction is achieved only by mechanical means and not inherently. The study of Ludwig Prandtl's 1933 theory of bell-shaped lift distribution,[2] Fig. 8 and 9 minimizes induced drag and introduces a stabilizing yaw moment by reducing lift toward the wingtips and generating a small induced thrust component.[3] This aerodynamic method helps counteract adverse yaw without additional control surfaces or drag-inducing mechanisms.

The tailless flying wing structure also supports RCS reduction due to its smooth, continuous shape and the elimination of protruding surfaces,[4,5] and by generating lift throughout the body is capable of high altitude and payload mission profiles.

2. Related work

2.1 Horten Ho 229 (Flying wing concept)

The Horten Ho 229 was a German jet-powered flying wing developed during World War II. It featured a tailless configuration with a blended wing-body design to reduce aerodynamic drag and increase efficiency. The aircraft used a delta wing shape to enhance high-speed performance and maneuverability.[6]

The flying wing configuration eliminated vertical stabilizers, resulting in smooth surfaces that contributed to a lower radar cross-section (RCS) as shown in Fig. 2, providing early stealth characteristics. These design choices aimed to make the aircraft less detectable by enemy radar systems.

The Horten Ho 229 was intended for use as a stealth bomber and reconnaissance aircraft. It had a wingspan of 16.8 meters (55.4 feet) and a length of 7.47 meters (24.6 feet). The top speed was approximately 1,000 km/h (621 mph). Stealth capability was achieved through its aerodynamic layout and surface design, which reduced radar detectability.[7]

2.2 Northrop Grumman B-2 Spirit (Stealth Bomber)

The Northrop Grumman B-2 Spirit is a modern flying wing aircraft developed for low-observable, long-range strategic bombing. The aircraft eliminates vertical stabilizers and uses radar-absorbing materials (RAM) along with shaping techniques to minimize radar cross-section (RCS),[4] as illustrated in Fig. 2. Stability and control are maintained using an advanced fly-by-wire control system, compensating for the lack of traditional aerodynamic surfaces.

The B-2 features a flying wing configuration with an integrated fuselage and wings. Its stealth capability is achieved through the combination of RAM and geometrical shaping. The fly-by-wire system enables stable flight and precise maneuvering without conventional vertical or horizontal stabilizers.[5]

It is employed for strategic bombing and covert military operations, including Intelligence, Surveillance, and Reconnaissance (ISR) in contested airspace. The aircraft has a top speed of approximately 1,010 km/h (627 mph), a range of 11,000 km (6,835 miles), and a payload capacity of 18,000 kg (39,683 lbs). The radar cross-section is approximately 0.1 m^2.[5,8]

2.3 NASA Prandtl-D (Bell-shaped lift distribution test)

The NASA Prandtl-D is a flying wing UAV developed to experimentally validate Ludwig Prandtl's bell-shaped lift distribution theory.[6] The design features aerodynamic twist along the span to reduce lift at the wingtips, generating a small induced thrust component that passively counters adverse yaw. This configuration eliminates the need for traditional control surfaces by providing inherent aerodynamic stability.

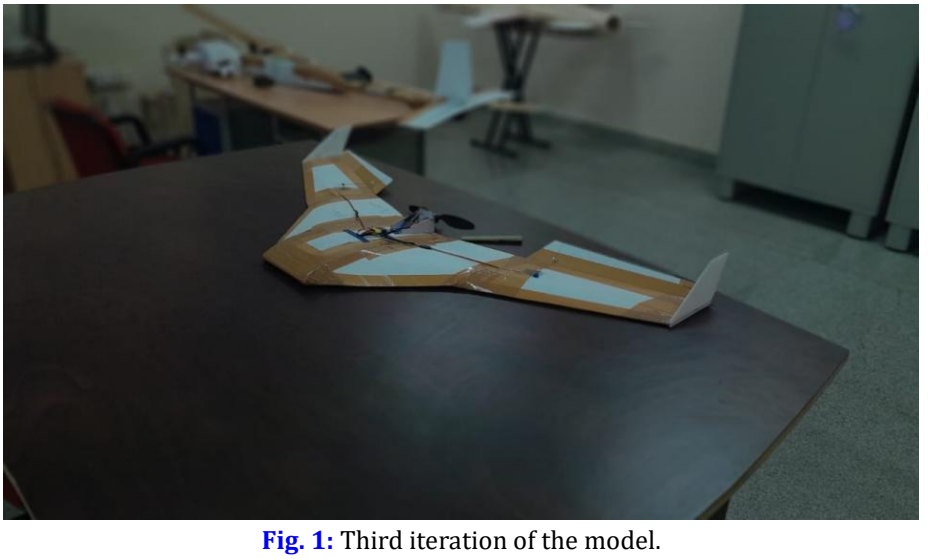


Fig. 1: Third iteration of the model.

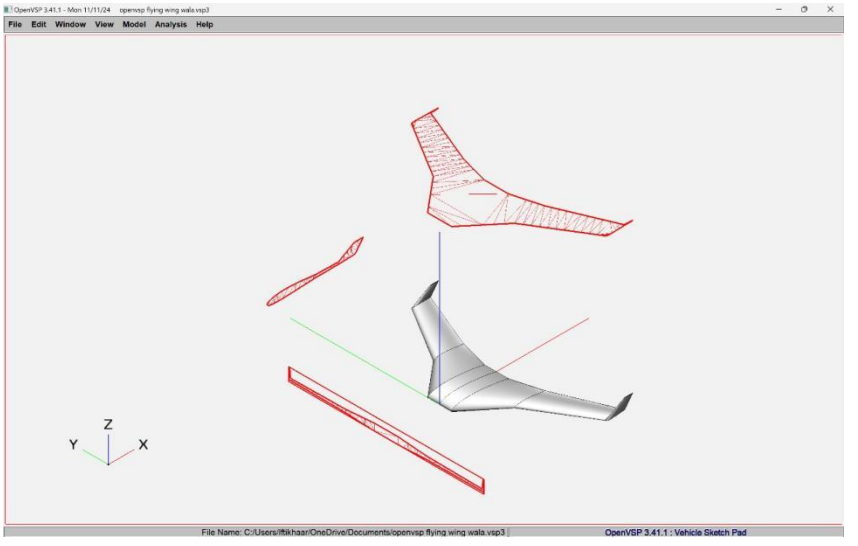


Fig. 2: Planform view showing minimum radar cross-section from front and side profiles.

The aircraft utilizes bell-shaped lift distribution in Figs. 8 and 9 to minimize induced drag. Spanwise twist reduces tip lift and creates a stabilizing thrust effect. Stability and control are achieved passively through aerodynamic shaping, without the use of active control surfaces.

The Prandtl-D was developed for research in tailless UAV and flying wing configurations, with particular application to long-endurance unmanned flight. The UAV has a wingspan of 25 feet (7.62 meters) and weighs 28 pounds (12.7 kg). Stability is maintained through passive aerodynamic design.[4]

2.4 Blended Wing Body (BWB) design

The Blended Wing Body (BWB) configuration integrates the wings and fuselage into a single, continuous lifting surface, eliminating the need for a conventional tail. This design as referred in Fig. 3 reduces aerodynamic drag, increases the lift-to-drag ratio, and improves fuel efficiency. It has been studied for both military and commercial aviation.[9]

The BWB features a seamless wing-fuselage structure that reduces drag and enhances lift. The aerodynamic benefits make it suitable for applications requiring high efficiency and long-range capability. The configuration supports both cargo and passenger layouts in commercial use, as well as strategic transport roles in military applications.

For example, the NASA X-48B demonstrator had a wingspan of 20.4 feet (6.2 meters), a gross weight of 523 pounds (237 kg), and used three small turbojet engines providing a combined thrust of approximately 160 pounds (72.6 kg).[10] Performance parameters vary depending on scale and mission requirements.

3. Research gap

Although flying wing designs have improved, there are still important problems related to structure, yaw control, and manufacturing accuracy. A major issue is the structural difficulty of using high aspect ratio wings, which are needed to apply bell-shaped lift distribution in Figs. 8 and 9 and reduce induced drag. When the aspect ratio increases, the bending moments at the wingtips also increase. This requires stronger materials and added reinforcement, which makes the structure heavier. High aspect ratio wings also have lower torsional stiffness,

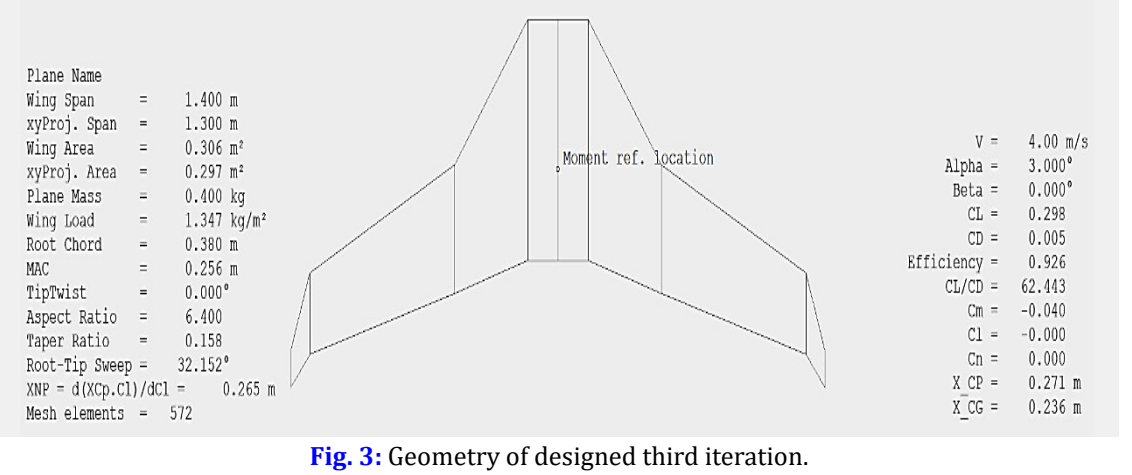


Fig. 3: Geometry of designed third iteration.

making them more likely to face aeroelastic problems such as flutter and divergence. For example, NASA's Prandtl-D, which was designed with bell-shaped lift distribution, failed in field tests because the wing tips did not have enough torsional strength.

Another flaw is active yaw instability. Since flying wing aircraft do not have vertical stabilizers, they cannot maintain yaw stability passively. Aircraft like the B-2 Spirit solve this using active systems. One method is split brake-rudders, placed on the outer trailing edges of the wing or by using winglets (Fig. 4). These can open on one side to create yawing force. Another method is differential thrust, where engine power is adjusted between the left and right sides to change direction. These systems work but require complex fly-by-wire (FBW) control. This adds electronic dependence and may reduce reliability, especially in environments where electronics can be jammed or damaged.

Attaining the required bell-shaped lift distribution demands precise aerodynamic or geometric twist along the wing span. This necessitates maintaining extremely tight manufacturing tolerances, often within sub-millimeter precision, across large-scale composite structures—a process that is both technologically demanding and cost-intensive. Additionally, ensuring structural continuity while integrating varying airfoil sections along the span, Fig. 3 presents significant engineering challenges. These factors collectively elevate production costs and can lead to compromises in aerodynamic performance if not addressed with high-precision fabrication and assembly techniques.

4. Proposed methodology

The objective is to develop a modular, aerodynamically stable tailless UAV architecture that integrates the bell-shaped lift distribution concept from Prandtl's 1933 theory[6,11] into a structurally optimized blended-wing airframe (Fig. 3). This design avoids reliance on mechanical yaw-control systems and mitigates the structural drawbacks of high aspect ratio flying wings by combining swept outer sections[7] with a low-aspect-ratio central lifting body.

The airframe comprises three primary aerodynamic zones. The central segment is a fuselage-integrated lifting body[1] with a low aspect ratio as seen at the center section of Fig. 3, serving as the main load-bearing structure. It accommodates internal payloads, avionics, and power systems, while concentrating bending stresses to preserve stiffness and reduce reinforcement in the outer wings.

The outer wing sections are swept and of higher aspect ratio[4,11] as seen at the center section of Fig. 3, with geometric washout achieved via twist and airfoil variation. This configuration induces a bell-shaped spanwise lift distribution,[6] reducing lift at the tips and generating an induced thrust component.[4] Adverse yaw is passively suppressed, eliminating the need for vertical stabilizers, drag rudders, or differential thrust.

Transition regions between the central body and outer panels are aerodynamically blended[9] to reduce vortex generation and maintain laminar flow. The blended-body planform[12] minimizes RCS (Fig. 2) through continuous curvature and the absence of upright surfaces. Structural loads are concentrated in the central body, offloading torsional stress from the slender outer panels.

Yaw and pitch control are achieved via integrated elevons along the trailing edge. No dedicated yaw-control surfaces are required as shown in Fig. 7. Stability augmentation, if necessary, is limited to minimal electronic correction, avoiding fully active fly-by-wire systems.

The design is modular and scalable. The central body and washout profile remain fixed, while outer wing span and sweep may be modified to suit mission-specific requirements.

5. Implementation stages

5.1 Stage 1: Determining the sweep angle for static directional stability

Objective: To determine the optimal sweep angle (Λ)

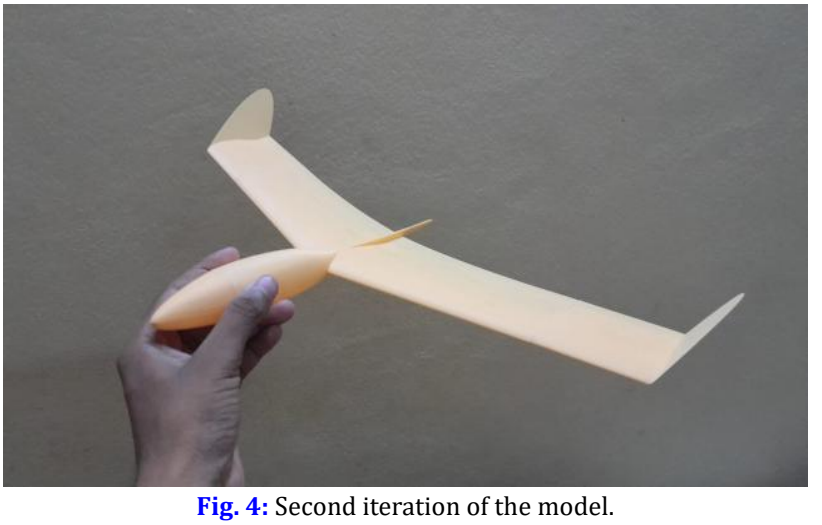


Fig. 4: Second iteration of the model.

that enhances static directional stability by leveraging the differential lift distribution caused by sideslip in a swept-wing configuration.

5.1.1 Effective angle of attack in sideslip

In a sideslip condition, the effective angle of attack (α_{eff}) varies along the span of a swept wing. For a given sideslip angle (β), sweep angle (Λ), and nominal angle of attack (α), the effective angle of attack at a spanwise location y is given by:

$$\alpha_{eff}(y)=\arctan\left(\frac{\sin\alpha\cos\beta}{\cos\alpha\cos\beta\cos\Lambda-\sin\beta\sin\Lambda}\right) \quad (1)$$

where,

α = nominal angle of attack

β = sideslip angle

Λ = sweep angle

This general expression accounts for the complete 3D velocity components relative to the swept wing section and is derived without small-angle or linear approximations. It reflects the variation of effective angle of attack across the span, which contributes to differential lift and results in rolling and yawing moments that influence directional stability (Fig. 7).

5.1.2 Lift curve slope reduction due to sweep

The lift curve slope ($\frac{dC_L}{d\alpha}$) of a wing is influenced by its aspect ratio (A) and quarter-chord sweep angle ($\Lambda_{1/4}$). For a swept wing in incompressible flow, the lift curve slope is reduced from the two-dimensional airfoil value (a_0) due to both three-dimensional finite wing effects and sweep.

$$\frac{dC_L}{d\alpha}=\frac{a_0\cos\Lambda_{1/4}}{1+\frac{a_0}{\pi A}} \quad (2)$$

where,

a_0 = two-dimensional lift curve slope (per radian)

A = wing aspect ratio

$\Lambda_{1/4}$ = quarter-chord sweep angle

*For an infinite swept wing, the lift curve slope reduces to:

$$\frac{dC_L}{d\alpha}_{\text{infinite}}=a_0\cos^2\Lambda_{1/4} \quad (3)$$

This expression accounts for the effective reduction in angle of attack and dynamic pressure experienced by each airfoil section due to sweep, as well as the spanwise lift distribution effects due to finite aspect ratio. It leads to a more gradual increase in lift with angle of attack.

5.1.3 Induced rolling moment and yawing moment

The differential lift and drag distributions along the span of a swept wing result in both rolling and yawing moments. These arise due to variations in effective angle of attack caused by sweep, twist, and sideslip.

5.1.3.1 Rolling moment

The rolling moment (L) generated by differential lift distribution is given by:

$$L=-\int_{-b/2}^{b/2} y\ C_L(y,\alpha_{eff}(y))\ q_\infty\ c(y)\ dy \quad (4)$$

where,

y = spanwise coordinate,

$C_L(y,\alpha_{eff}(y))$ = local section lift coefficient,

$q_\infty=\frac{1}{2}\rho V_\infty^2$ = freestream dynamic pressure,

c(y) = local chord length.

This moment arises as the product of lift force and its moment arm about the roll axis. It stabilizes the aircraft against sideslip by generating an opposing roll.

5.1.3.2 Yawing moment

The yawing moment (N) arises due to the sweep-induced lateral component of lift and the longitudinal component of drag. It is given by:

$$N=\int_{-b/2}^{b/2}\left[(x_{QC}(y)-x_{CG})\ C_L(y,\alpha_{eff}(y))\sin(\Lambda(y))+y\ C_D(y,\alpha_{eff}(y))\cos(\Lambda(y))\right] q_\infty\ c(y)dy \quad (5)$$

where,

x_{QC} (y) = quarter-chord x-location at spanwise station y,

x_{CG} = x-location of the center of gravity,

$C_D(y,\alpha_{eff}(y))$ = local section drag coefficient,

$\Lambda(y)$ = local sweep angle.

The first term reflects the yawing moment due to spanwise lift components at a distance from the CG, while the second term captures yawing due to drag forces at outboard span stations.

These integrals can be evaluated numerically or approximated under linear assumptions for analytical design.

5.2 Stage 2: Determining the planform, aerodynamic center, and center of gravity

Objective: To design a balanced wing planform that ensures the aerodynamic center (AC) and center of gravity (CG) are optimally positioned to achieve desired static stability and control.

5.2.1 Planform Geometry and Mean Aerodynamic Chord (MAC)

Mean Aerodynamic Chord (MAC): The Mean Aerodynamic Chord (MAC) is a fundamental parameter used to define the average chord length weighted by aerodynamic effect, as implemented in the final planform in Fig. 3. For a trapezoidal wing with root chord c_{root} and tip chord c_{tip}, the MAC is calculated as:

$$\bar{c}=\frac{2}{3}\cdot\frac{c_{root}^2+c_{root}\cdot c_{tip}+c_{tip}^2}{c_{root}+c_{tip}} \quad (6)$$

where,
c_{root} = root chord length
c_{tip} = tip chord length
This expression accounts for the chord variation along the span and is valid for any symmetric trapezoidal wing geometry. It is derived from first principles by integrating the square of the local chord along the span and normalizing by the wing area.
Aerodynamic Center (AC): For a symmetric airfoil, the aerodynamic center is located at 25% of the MAC from the leading edge.

5.2.2 Center of Gravity (CG) calculation

CG Calculation: The CG is the weighted average location of all mass elements in the aircraft. For components i with mass m_i and distance x_i from a reference point, the CG is:

$$x_{CG}=\frac{\sum m_i \cdot x_i}{\sum m_i} \quad (7)$$

Component Masses:
Wing Mass: $m_{wing}=\rho_{material} \cdot S_{wing} \cdot t_{wing}$
Payload Mass: $m_{payload}=\rho_{payload} \cdot S_{payload} \cdot t_{payload}$
Propulsion System Mass:
$m_{propulsion}=\rho_{propulsion} \cdot S_{propulsion} \cdot t_{propulsion}$
where,
ρ = density of the material,
S = surface area,
t = thickness of the component.

5.2.3 Neutral Point (NP) and static margin

Neutral Point (NP): The neutral point is the longitudinal position about which the pitching moment coefficient remains constant with changes in angle of attack. It represents the boundary between static stability and instability and, for an aircraft to be statically stable, the center of gravity must lie ahead of the neutral point.
For a complete aircraft, the NP is given by:

$$x_{NP}=x_{AC}+\frac{V_H \cdot a_s}{a_w} \cdot \left(1-\frac{\partial \epsilon}{\partial \alpha}\right) \quad (8)$$

where,
x_{AC} = aerodynamic center of the wing,
$V_H=\frac{S_H l_H}{S\bar{c}}$ = tail volume ratio,
a_s , a_w = lift curve slopes of the stabilizer and wing, respectively,
$\frac{\partial \epsilon}{\partial \alpha}$ = downwash gradient (effect of wing on tail angle of attack).
For an isolated wing, the NP coincides with the aerodynamic center. Its exact location for a swept trapezoidal wing is given by:

$$x_{NP}=x_{AC}=\frac{\int_{-b/2}^{b/2}\left(x_{LE}(y)+\frac{1}{4}c(y)\right)c(y)\frac{dc_l(y)}{d\alpha}dy}{\int_{-b/2}^{b/2}c(y)\frac{dc_l(y)}{d\alpha}dy} \quad (9)$$

where, $x_{LE}(y)=x_{LE,root}+|y|\tan\Lambda_{LE}$ - longitudinal position of the leading edge at spanwise station y,
$c(y)=c_r-(c_r-c_t)\frac{|y|}{b/2}$ - local chord length at y for a trapezoidal wing,
$\frac{dc_l(y)}{d\alpha}$ - local lift curve slope at y,
b - total wingspan,
c_r, c_t - root and tip chords, respectively.
Static Margin (SM): The SM is the distance between the CG and NP, normalized by the MAC:

$$SM=\frac{x_{NP}-x_{CG}}{\bar{c}} \quad (10)$$

A positive SM indicates a statically stable aircraft, as verified in the stability analysis (Fig. 5 and Fig. 7).

5.3 Stage 3: Airfoil selection, washout implementation, and lift distribution optimization

Objective: To design a wing with a reflexed airfoil configuration and a washout distribution that minimizes induced drag and ensures stable aerodynamic performance, utilizing Prandtl's 1933 solution for lift distribution.

5.3.1 Airfoil selection: reflexed airfoils

Reflexed airfoils are used in flying wing designs to achieve pitch stability,[13] with performance characteristics shown in Fig. 5 and Fig. 6, without a horizontal stabilizer. These airfoils generate a negative pitching moment at zero lift, which helps maintain pitch stability through aerodynamic means.[1] In addition to stability, reflexed airfoils can improve aerodynamic efficiency by reducing drag at higher angles of attack. This is achieved by delaying the onset of flow separation. For design, several factors must be considered. The camber line of the airfoil must be shaped to produce a negative pitching moment at zero lift.[13] The thickness-to-chord ratio should be moderate, as demonstrated by the NACA 2412 and MH60 airfoils in Fig. 6 to provide a balance between structural strength and aerodynamic performance. Also, the airfoil must be compatible with the operating Reynolds number range, which for small UAVs is typically between 10^5 and 10^6 Performance outside this range can lead to reduced efficiency or loss of control.

5.3.2 Washout implementation

Washout is the reduction in the angle of attack from root to tip along the span of the wing and is responsible for the lower angle of attack being created at the tip[11,13] inducing a thrust component.
Twist Distribution: The twist angle (θ) at a spanwise location y can be defined as:

$$\theta(y)=\theta_{root}-\frac{y}{b} \cdot (\theta_{root}-\theta_{tip}) \quad (11)$$

where,
θ_{root} = twist angle at the root,

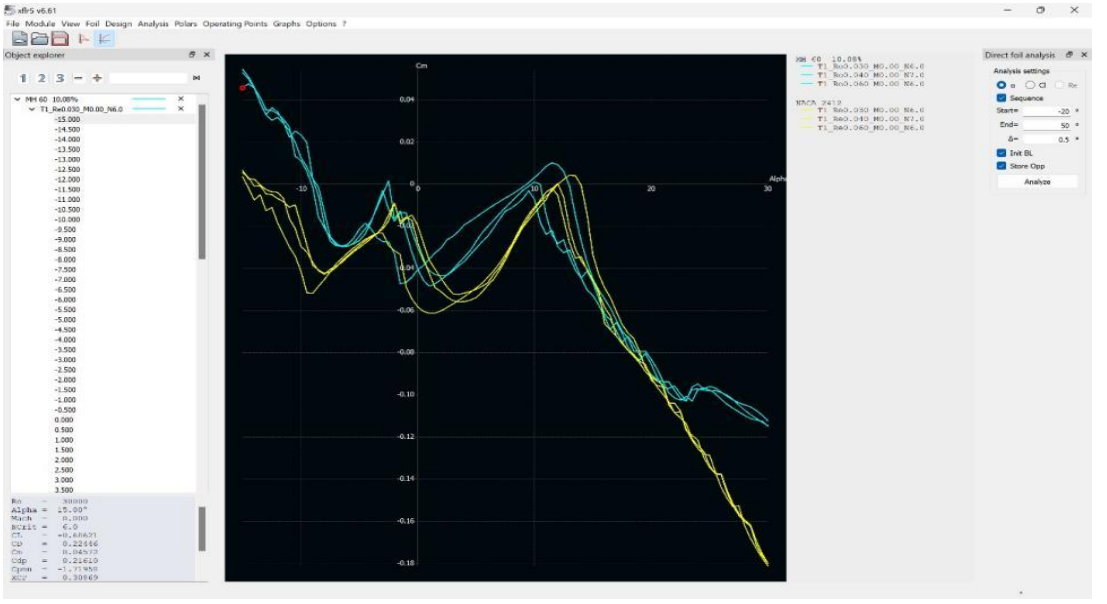


Fig. 5: Airfoil static stability (Blue = MH60, Yello = NACA 2412.

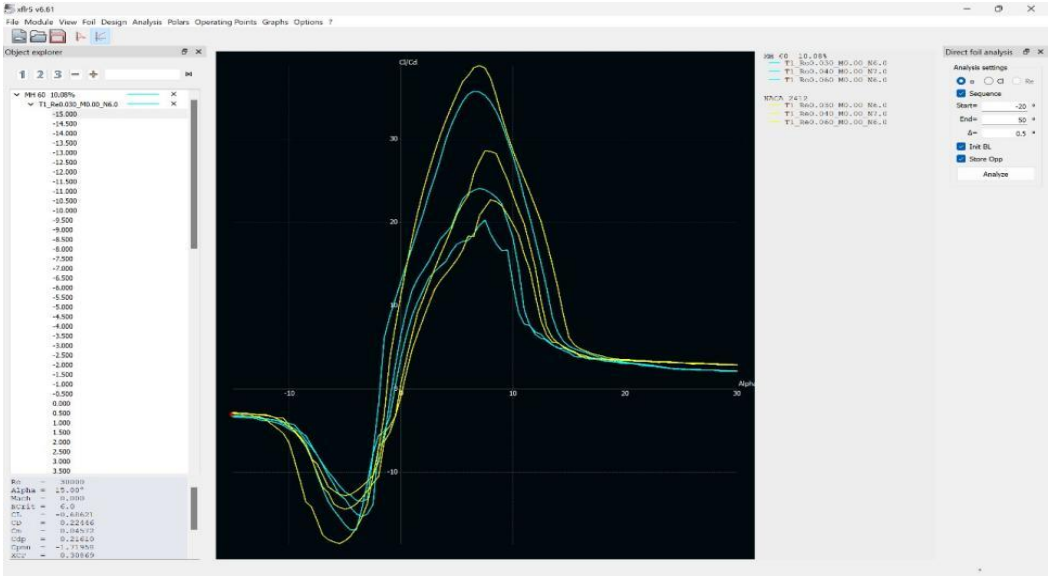


Fig. 6: Airfoil aerodynamic efficiency (Blue = MH60, Yello = NACA 2412).

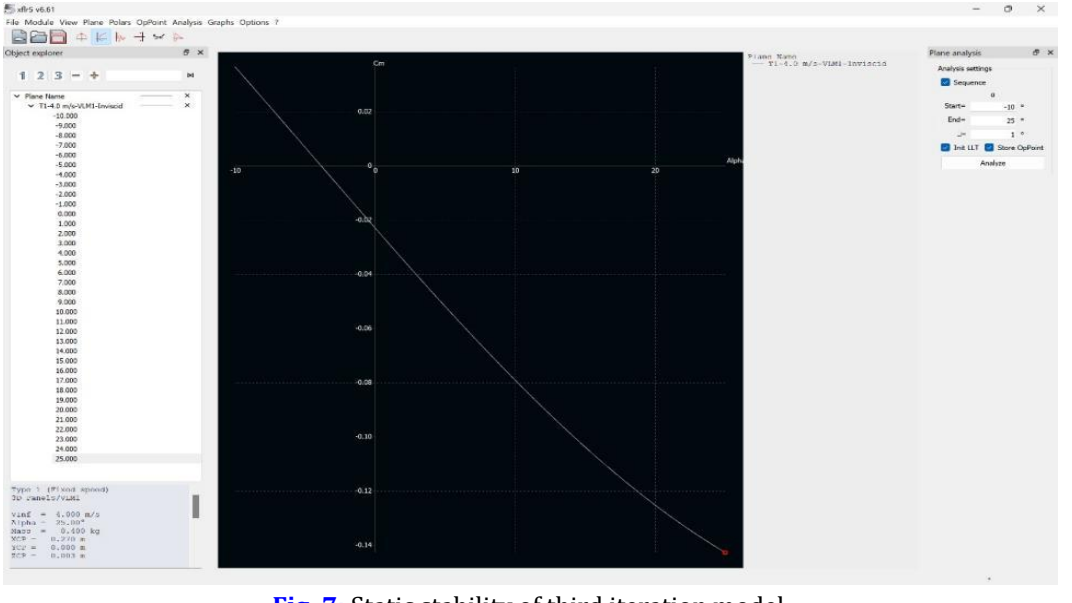


Fig. 7: Static stability of third iteration model.

θ_{tip} = twist angle at the tip,
b = wingspan.
This washout is analyzed by performing a VLM and LLT (Vortex Lattice Method, Lifting Line Theory) analysis to evaluate the aerodynamic characteristics and ensure that the washout distribution leads to the desired lift distribution and stability.

5.3.3 Prandtl's bell-shaped lift distribution (1933 Solution)

Prandtl proposed an alternative lift distribution in 1933, known as the bell-shaped lift distribution,[11] which also achieves minimum induced drag but produces different rolling moment characteristics-particularly beneficial for tailless aircraft and flying wings.
The non-dimensional lift distribution in terms of angle θ is:

$$\frac{\tilde{L}(\theta)}{L}=\frac{4}{\pi}\left(\sin(\theta)-\frac{1}{3}\sin(3\theta)\right) \quad (12)$$

where,
$\tilde{L}(\theta)$ is the local sectional lift,
L is the total lift,
θ is a spanwise location angle defined by:

$$y=-\frac{b}{2}\cos(\theta), \quad \theta\in[0,\pi]$$

b is the total wingspan.

Interpretation:

In lifting line theory, this corresponds to a specific combination of Fourier coefficients:

$$B_1=1, \quad B_3=-\frac{1}{3}, \quad B_n=0 \text{ for } n\neq 1,3$$

By setting $B_n=0$ for n>3, induced drag remains minimized under the fixed wingspan and lift constraint, but the resulting lift distribution reduces tip loading and rolling moments.

Prandtl's bell-shaped lift distribution was later found to be advantageous in designs like the Horten flying wing. The key difference from the elliptical lift distribution is the reduced lift at the wingtips, leading to lower vortex strength and reduced roll-yaw coupling.

5.4 Stage 4: Fluid simulation, design finalization, and integration

5.4.1 Fluid simulation for aerodynamic testing

Objective: To perform fluid simulations for induced drag, downwash, and lift distribution, ensuring the optimized aerodynamic characteristics of the design are validated before physical testing.

The computational fluid dynamics (CFD) simulation setup is carried out using suitable software platforms such as ANSYS Fluent, OpenFOAM, or XFLR5. These tools are selected based on availability and compatibility with the modeling requirements, producing results as shown in Figs. 8, 9 and 12 of the tailless UAV configurations. A

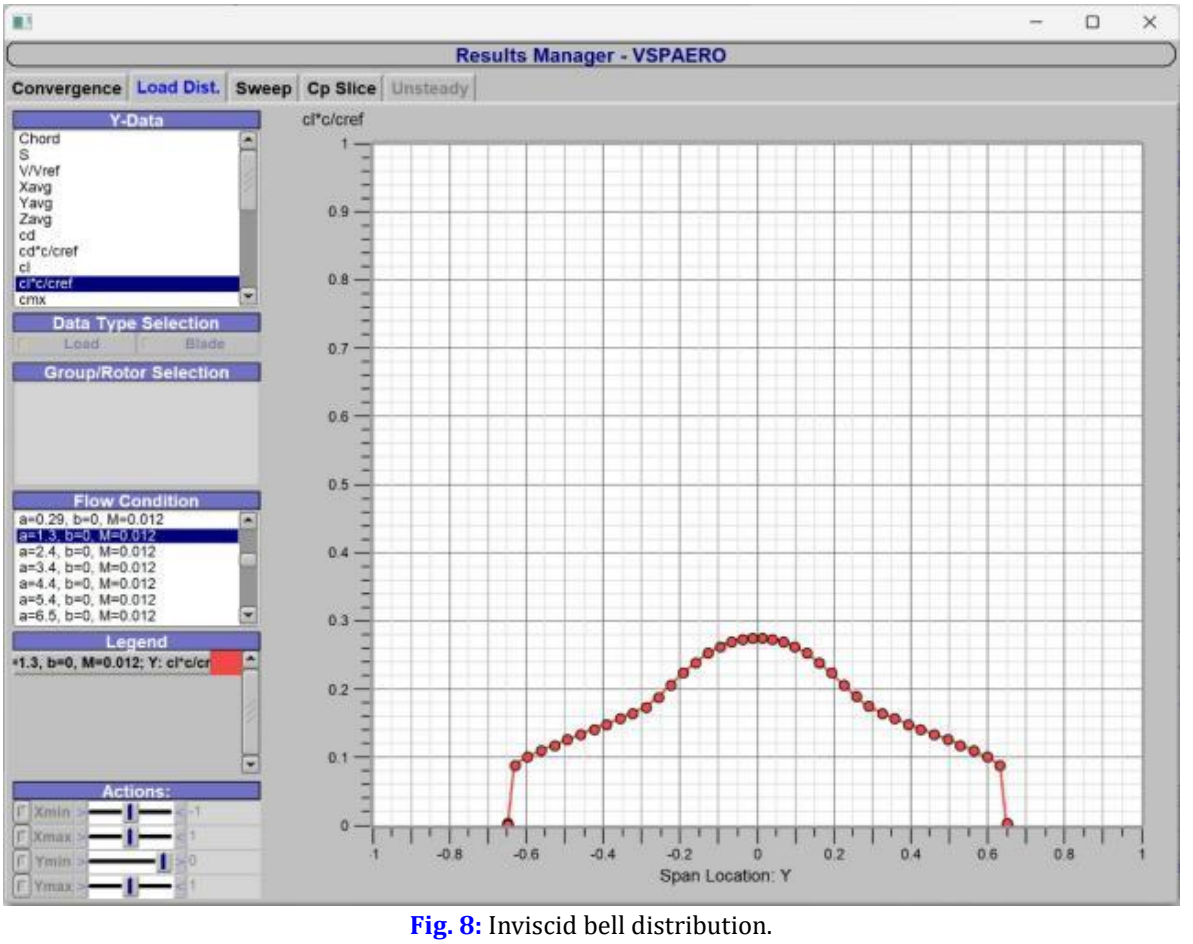


Fig. 8: Inviscid bell distribution.

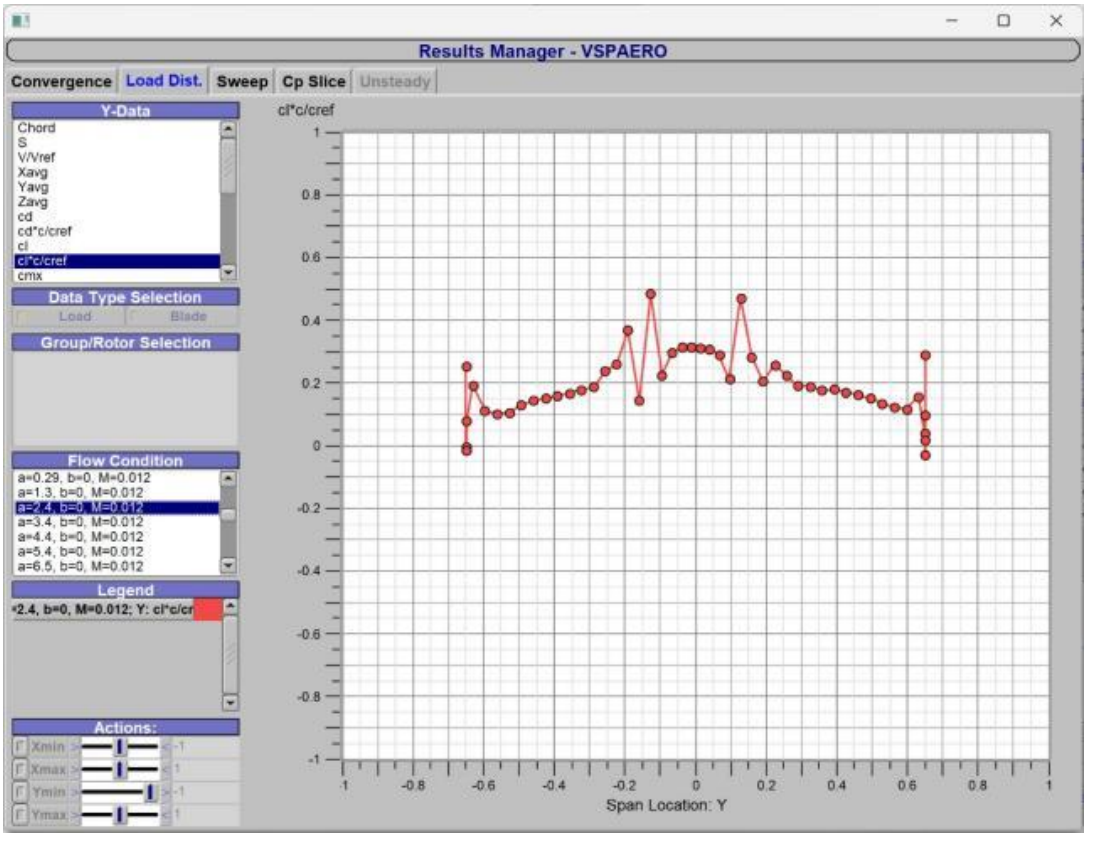


Fig. 9: Viscous bell distribution.

refined mesh is generated to capture the geometric and aerodynamic surface features of the wing and its surrounding flow field. Mesh density is increased near critical regions such as the leading edge, trailing edge, and wing tips to accurately resolve vortex structures, pressure gradients, and boundary layer behavior.

Boundary conditions are defined to reflect realistic flight scenarios. The inlet boundary is set with a free-stream velocity corresponding to the desired flight condition. At the outlet, a pressure outlet boundary is applied to allow airflow to exit the computational domain smoothly. All surfaces of the wing are treated with a no-slip wall condition to simulate realistic flow interaction with the solid boundary.

Flow parameters are assigned based on the targeted flight regime. These include setting the Mach number, Reynolds number, and angle of attack in accordance with the expected operating envelope. These inputs ensure that the simulation reflects the aerodynamic behavior of the design under practical conditions, enabling assessment of lift distribution, induced drag, and flow separation patterns.

Simulation Parameters: To identify negative downwash (i.e., upwash at the tips) and to minimize induced drag C_{D_i} , the following aerodynamic relationships are employed:

a) Induced drag (Lift-induced drag calculation):

The general expression for the induced drag coefficient, without assuming elliptical lift distribution, is derived from Prandtl's lifting line theory:

$$C_{D_i} = \frac{2}{V_\infty^2 S} \int_{-b/2}^{b/2} \Gamma(y)\, w_i(y)\, dy \quad (13)$$

where,

$\Gamma(y)$ is the circulation distribution along the span,

$w_i(y)$ is the downwash velocity at spanwise location y, given by:

$$w_i(y) = \frac{1}{4\pi} \int_{-b/2}^{b/2} \frac{d\Gamma(y')/dy'}{y-y'}\, dy' \quad (14)$$

S is the wing planform area,

V_∞ is the freestream velocity.

The lift coefficient is related to the circulation distribution as:

$$C_L = \frac{2}{V_\infty S} \int_{-b/2}^{b/2} \Gamma(y)\, dy \quad (15)$$

For wings with **elliptical lift distribution**, the downwash becomes spanwise constant, and the induced drag coefficient simplifies to the classical expression:

$$C_{D_i} = \frac{C_L^2}{\pi \cdot AR \cdot e} \quad (16)$$

where,

$AR = \frac{b^2}{S}$ is the aspect ratio,

e is Oswald's efficiency factor (typically 0.7–1.0).

This formulation, both general and approximate, is used to evaluate aerodynamic efficiency as shown in Fig. 10.

b) Downwash calculation

The downwash at each spanwise location y is determined

by the distribution of circulation Γ(y) shed from the trailing edge. For a swept wing with variable airfoil geometry, the general expression derived from Biot-Savart law is:

$$w_i(y)=-\frac{1}{4\pi}\int_{-b/2}^{b/2}\frac{d\Gamma(y')/dy'}{y-y'}\,dy' \quad (17)$$

The corresponding induced angle of attack at spanwise location y is:

$$\alpha_i(y)=\frac{w_i(y)}{V_\infty} \quad (18)$$

The effective angle of attack becomes:

$$\alpha_{eff}(y)=\alpha_g(y)\cos\Lambda(y)-\frac{w_i(y)}{V_\infty} \quad (19)$$

and the local circulation, incorporating sweep effects, becomes:

$$\Gamma(y)=\frac{1}{2}V_\infty c(y)a_0(y)\left(\alpha_g(y)-\frac{w_i(y)}{V_\infty}\right)\cos\Lambda(y) \quad (20)$$

Lift Distribution: Use XFLR5 or similar tools to simulate the lift distribution, ensuring results match the optimal pattern shown in Figs. 8 and 9 along the span of the wing. Ensure that the distribution follows the optimal Prandtl's solution,[11] with a reduced lift toward the wingtips.

c) Iterations and validation

The simulation process involves multiple iterations wherein the wing twist distribution and airfoil sectioning are adjusted to achieve the target lift distribution and minimize induced drag. Each iteration includes evaluation of the flow field, with particular attention to vortex shedding behavior and vortex-induced drag, to verify that the configuration supports low-drag, stable flight. Modifications are made incrementally based on observed aerodynamic performance metrics until the simulation output aligns with the predefined criteria.

In addition to general aerodynamic validation, the effects of downwash are assessed to understand their impact on the flow structure and pressure distribution. This includes analyzing how the wing's trailing flow interacts with any downstream control surfaces or structures, such as a tail section if present, to ensure that induced flow does not degrade stability or control effectiveness.

5.4.2 Structural design finalization

After validating the aerodynamic characteristics, the structural design is finalized. The wing is divided into panels based on the final aerodynamic shape illustrated in Fig. 3. Each panel must follow the airfoil geometry and the twist distribution across the span. The wing skin is designed accordingly, using lightweight and high-strength materials such as carbon fiber composite or fiberglass, which provide the necessary strength-to-weight ratio for UAV applications. Internally, the wing includes a structural skeleton made up of formers or ribs that define the airfoil shape and provide mechanical strength. These internal members are constructed from materials like aluminum alloy or carbon fiber, and they are spaced at regular intervals to maintain structural integrity and preserve the aerodynamic profile.

Once the skeleton is complete, the skin panels are applied using adhesive bonding methods. Care is taken to align each panel precisely along the aerodynamic surface to ensure smooth transitions between them, minimizing drag and maintaining the aerodynamic performance established.

5.4.3 Prototype testing (free-glide tests)

Objective: To validate the aerodynamic characteristics and structural integrity through free-glide tests.

Procedure: Initial testing involves performing free-glide trials using the prototypes similar to those shown in Figs.

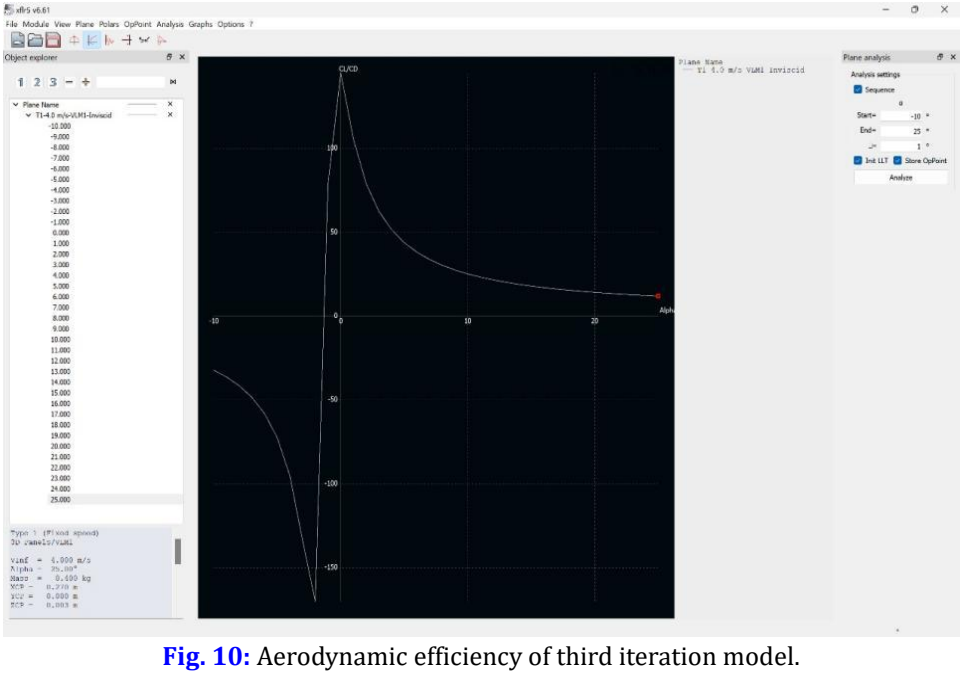


Fig. 10: Aerodynamic efficiency of third iteration model.

4 and 1, with an additional ballast installed to simulate the weight of onboard electronics and payload. These tests are designed to evaluate whether the aircraft can maintain stable, unpowered flight. During each trial, the glide path is observed and recorded to identify any deviations from the expected trajectory. Deviations are used to inform necessary adjustments to the airframe geometry or control configuration.

Tests are conducted under calm weather conditions, free of significant crosswinds or gusts, to ensure that environmental factors do not affect the assessment. The aircraft's response to small, deliberate perturbations is observed to assess its inherent stability and control behavior in an unpowered state.

Feedback: Data obtained from the gliding tests, including glide path characteristics and stability metrics, are used to refine the design. Modifications may include adjusting the geometric washout or selecting alternate airfoil sections to improve stability or performance as required.

5.4.4 Integration with electronics and propulsion unit

Objective: To integrate the necessary flight control electronics and propulsion unit for powered flight.

Procedure: The integration phase begins with the installation of a flight control unit (FCU) capable of managing aircraft stability in pitch, roll, and yaw. For the tailless configuration, the control surfaces must be configured to produce minimal drag while ensuring sufficient authority over the flight axes. Inertial Measurement Units (IMUs) and a GPS module are incorporated to provide real-time data for navigation and control.

A fly-by-wire system is implemented to manage stability and dynamic response in real-time, ensuring reliable control without mechanical linkage systems. The propulsion unit is selected based on the required thrust-to-weight ratio. For this class of UAV, the system typically comprises compact brushless motors and high-efficiency propellers. The propulsion system is connected to the FCU, enabling coordinated control of throttle and aerodynamic surfaces for stable powered flight.

After integration, ground tests are conducted to verify that all electronic systems function correctly. This is followed by powered testing to validate that the propulsion unit is operating in synchronization with the control system. Control software parameters are then calibrated and fine-tuned based on performance under different flight conditions.

6. Result

Three iterations were carried out to evaluate the capability and feasibility of the proposed plan. Two airfoils in Fig. 6 were selected for the final design: NACA 2412 at the main body and MH60 at the wing tips to incorporate geometric twist and washout. The first iteration (Fig. 11) focused on testing static stability and overall balance while refining the planform. In the second iteration (Fig. 4), the planform was revised and winglets were added at a 72° angle to improve directional stability through circulation. This version was designed for hand launch to observe stability behavior. The third iteration as shown in Fig. 1 was developed entirely using simulation tools and CFD analysis. According to the simulation data, a bell-shaped lift distribution was achieved in both inviscid in Fig. 8 and viscous flow in Fig. 9 conditions, also shown in the coefficient of pressure plot in Fig. 12. As shown in Figs. 5 and 7, the aircraft exhibited static stability without a tail, confirming the feasibility of tailless flight. Additionally, the aerodynamic performance of the airfoils and the overall design showed high lift-to-drag ratios at angles of attack below 7° as in

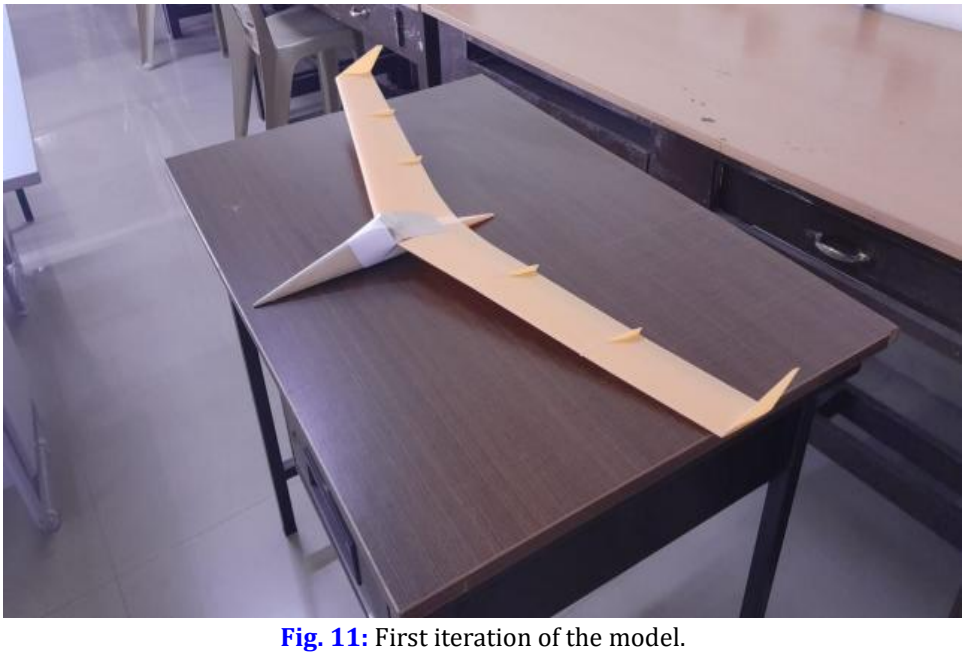


Fig. 11: First iteration of the model.

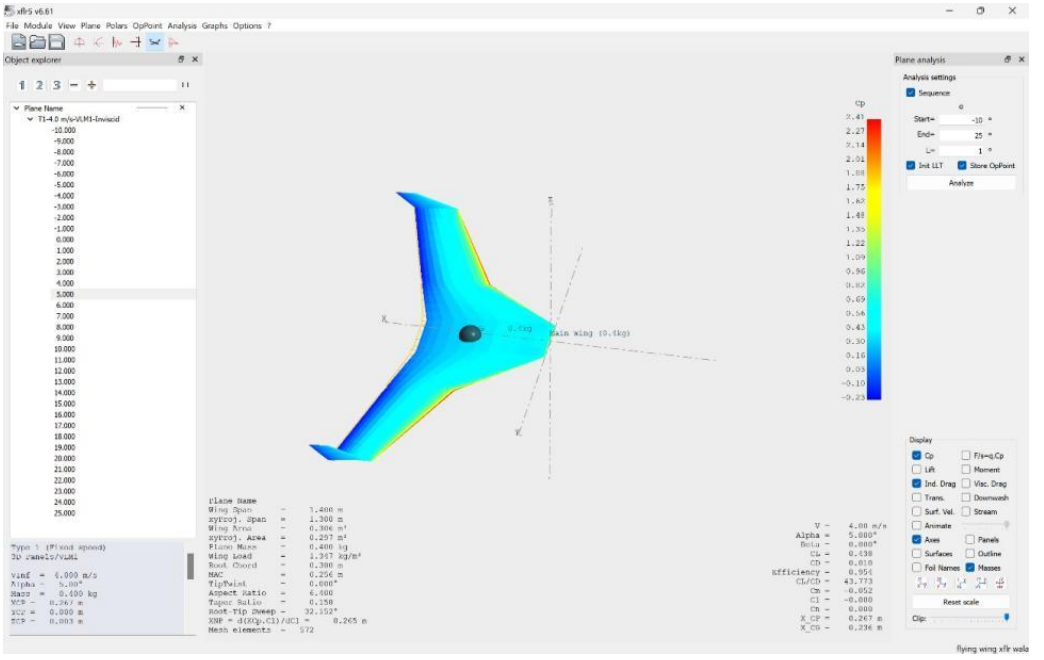


Fig. 12: CP plot showing bell distribution.

Figs. 6 and 10. This third design in Fig. 2 was later modified into a radio-controlled prototype as shown Fig. 1 and featured a blended wing configuration with incorporated washout.

7. Conclusion

This study successfully demonstrates the feasibility of a tailless flying wing UAV optimized for low radar cross-section and aerodynamic stability using Prandtl's bell-shaped lift distribution in Fig. 12. Through three design iterations in Fig. 11, Fig. 4 and Fig. 1, the final configuration employed geometric twist using NACA 2412 and MH60 airfoils (Fig. 6, Fig. 5), to achieve a stable lift distribution with reduced induced drag (Fig. 10). CFD simulations confirmed bell-shaped lift behavior in both inviscid and viscous flows (Fig. 8 and Fig. 9), and verified that the design remains statically stable without a vertical tail (Fig. 7). The aircraft also exhibited high lift-to-drag ratios below 7° angle of attack, validating aerodynamic efficiency (Fig. 10). The final prototype incorporated a blended wing configuration with washout and was realized as a functional radio-controlled platform (Fig. 3 and Fig. 1). These results confirm that passive aerodynamic control through spanwise load redistribution can reduce reliance on active yaw stabilization systems, making this approach viable for ISR and stealth missions where structural simplicity and low observability are critical (Fig. 2). Despite these promising results, several challenges must be addressed for real-world deployment. The implementation of precise geometric twist and spanwise airfoil variation requires tight manufacturing tolerances, particularly in composite structures, which can significantly increase fabrication complexity and cost. Moreover, the absence of vertical stabilizers limits passive yaw damping, necessitating robust control algorithms and redundant sensor systems to maintain directional stability under crosswind and turbulence. Structural flexibility and aeroelastic effects, such as wing twist under load or flutter, must also be carefully analyzed and mitigated during scaling. Future work should focus on system-level integration, hardware-in-the-loop testing, and flight validation under diverse conditions for full-scale deployment.

Funding Declaration

This research did not receive any specific grant from funding agencies in the public, commercial, or not-for-profit sectors.

Data Availability Statement

The data supporting the findings of this study are available within the article. Additional data related to the UAV design, aerodynamic analysis, and CFD simulations are available from the corresponding author upon reasonable request.

Conflict of Interest

There is no conflict of interest.

Artificial Intelligence (AI) Use Disclosure

The authors declare that artificial intelligence (AI)-assisted tools were used only for language refinement, grammar improvement, and manuscript structuring purposes during the preparation of this work. All technical content, analysis, and interpretations were independently developed and verified by the authors.

Supporting Information

Not applicable.

References

[1] Aviation Stack Exchange contributors, How does wing sweep increase aircraft stability? 2015, aviation Stack Exchange, available at: https://aviation.stackexchange.com/questions/9287/how-does-wing-sweep-increase-aircraft-stability.

[2] A. H. Bowers, O. J. Murillo, R. Jensen, B. Eslinger, C. Gelzer, Spanload implications for aircraft and birds, NASA Technical Report No. 20160003578, 2016, available: https://ntrs.nasa.gov/api/citations/20160003578/downloads/20160003578.pdf.

[3] A. H. Bowers, O. J. Murillo, D. E. Berger, V. S. Hawkins, L. J. Newton, A. G. Waddell, E. D. Glover, J. C. Brady, J. K. Bodylski, R. Jensen, R. A. Bowers, C. Gelzer, D. R. Jackson, R. J. Suitor, Experimental flight validation of the Prandtl 1933 bell spanload, 2021, NASA Technical Memorandum No. 20210014683, available: https://ntrs.nasa.gov/api/citations/20210014683/downloads/H3284FINAL.pdf.

[4] Northrop b-2 spirit, 2024, Wikipedia article, available: https://en.wikipedia.org/wiki/Northrop B-2 Spirit.

[5] N. Arif, Performance analysis of b-2 spirits, College of Aeronautical Engineering, National University of Sciences and Technology, 2023.

[6] Horten ho 229, 2024, Wikipedia article, available: https://en.wikipedia.org/wiki/Horten Ho 229.

[7] National Air and Space Museum, Horten ho 229 v3, 2023, Smithsonian Institution, available: https://airandspace.si.edu/collection-objects/horten-ho-229-v3/nasm_A19600324000.

[8] John M. Griffin, James E. Kinnu, edited by John M. Colombi. 2007. B-2 Systems Engineering Case Study. Air Force Center for Systems Engineering at the Air Force Institute of Technology. Defense Technical Information Center Report ADA464771. Available: https://apps.dtic.mil/sti/tr/pdf/ADA464771.pdf.

[9] Blended wing body, 2024, Wikipedia article, available: https://en.wikipedia.org/wiki/Blended wing body.

[10] NASA, X-48b, 2024, NASA Aeronautics, available: https://www.nasa.gov/aeronautics/x-48b/.

[11] C. Robb, R. Paul, Aerodynamic modeling of a flying wing featuring ludwig prandtl's bell spanload, *Aerospace*, 2023, **10**, 613, doi: 10.3390/aerospace10070613.

[12] MH AeroTools, Flying wing design, 2024, mH AeroTools website, available: https://www.mh-aerotools.de/airfoils/flywing1.htm

[13] J. D. Hoyos, C. Echavarría, J. P. Alvarado, G. Su rez, J. A. Niño, J. I. García, Two-way coupled aero-structural optimization of stable flying wings, *Aerospace*, 2023, **10**, 346, doi: 10.3390/aerospace10040346.

Publisher Note: The views, statements, and data in all publications solely belong to the authors and contributors. GR Scholastic is not responsible for any injury resulting from the ideas, methods, or products mentioned. GR Scholastic remains neutral regarding jurisdictional claims in published maps and institutional affiliations.